Research Article Vol. 7, No. 10 / October 2020 / Optica 1445

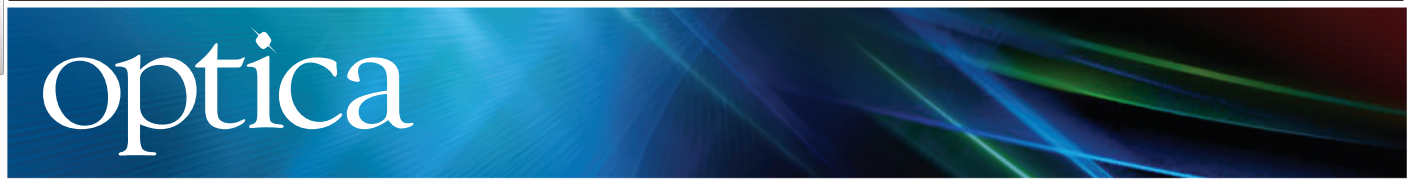

Ultra-high-resolution software-defined photonic terahertz spectroscopy

Rodolfo I. Hermans,[1,2] James Seddon,[2,*] Haymen Shams,[2] Lalitha Ponnampalam,[2] Alwyn J. Seeds,[2] and Gabriel Aeppli[3,4]

[1]London Centre for Nanotechnology, University College London, 17-19 Gordon Street, London WC1H 0AH, UK
[2]Department of Electronic and Electrical Engineering, University College London, Torrington Place, London WC1E 7JE, UK
[3]Departments of Physics, ETH Zürich, CH-8093 Zürich, Switzerland and École Polytechnique Fédérale de Lausanne (EPFL), CH-1015 Lausanne, Switzerland
[4]Photon Science Division, Paul Scherrer Institute, CH-5232, Villigen, Switzerland
*Corresponding author: a.seeds@ucl.ac.uk

Received 13 May 2020; revised 4 September 2020; accepted 4 September 2020 (Doc. ID 397506); published 16 October 2020

A novel technique for high-resolution 1.5 μm photonics-enabled terahertz (THz) spectroscopy using software control of the illumination spectral line shape (SLS) is presented. The technique enhances the performance of a continuous-wave THz spectrometer to reveal previously inaccessible details of closely spaced spectral peaks. We demonstrate the technique by performing spectroscopy on $LiYF_4:Ho^{3+}$, a material of interest for quantum science and technology, where we discriminate between inhomogeneous Gaussian and homogeneous Lorentzian contributions to absorption lines near 0.2 THz. Ultra-high-resolution (<100 Hz full-width at half maximum) frequency-domain spectroscopy with quality factor $Q > 2 \times 10^9$ is achieved using an exact frequency spacing comb source in the optical communications band, with a custom uni-traveling-carrier photodiode mixer and coherent down-conversion detection. Software-defined time-domain modulation of one of the comb lines is demonstrated and used to resolve the sample SLS and to obtain a magnetic field-free readout of the electronuclear spectrum for the Ho^{3+} ions in $LiYF_4:Ho^{3+}$. In particular, homogeneous and inhomogeneous contributions to the spectrum are readily separated. The experiment reveals previously unmeasured information regarding the hyperfine structure of the first excited state in the $^5I_8$ manifold complementing the results reported in Phys. Rev. B 94, 205132 (2016).

https://doi.org/10.1364/OPTICA.397506

1. INTRODUCTION

The terahertz (THz) electromagnetic band (0.1 THz to 10 THz) lies in the technically challenging spectral gap between infrared light and microwave radiation [1,2]. Specialized technology for the generation, manipulation, and detection of so-called "T-rays" has come later than for other frequency bands and is still an active area of development. The THz regime offers many opportunities. For example, THz radiation is mainly innocuous to live tissue [3], making it attractive for medical diagnostics and material identification for safety and security. Despite the significant absorption of THz radiation by the atmosphere, existing transmission windows also allow useful applications in astronomy [4] and telecommunications [5]. Finally, various THz excitations in solids offer promise for quantum measurement and control [6], if compact coherent sources could be realized.

Astronomy has been a key driving force in the development of THz sources for observations of the C I, C II, CO, and, O I spectral lines, which all lie in the THz region. Heterodyne mixers are the most commonly deployed technology in several astrophysics missions where Schottky diode multipliers are used as the local oscillator (LO) to drive Schottky diode mixers [7], superconductor–insulator–superconductor mixers [8–10], and hot electron bolometer mixers [11–13]. Ultra-narrow-linewidth multiplier sources have been demonstrated for high-resolution spectroscopy of molecular species [14]. The phase noise of multiplier sources is primarily dependent on the number of multiplication steps N in the multiplier chain, adding a $20 \log_{10}(N)$ penalty to the phase noise of the source generator. The tuning range of frequency multiplier sources is also limited to discrete frequency bands of less than one octave, set by the rectangular waveguides the multiplier diodes are commonly packaged in.

THz spectroscopy is currently dominated by Fourier transform infrared (FTIR) [15] and time-domain spectroscopy (TDS). Off-the-shelf FTIR spectrometers such as the Bruker IFS 125HR FTIR claim broad spectral range from 5 cm^{-1} (2 mm, 149.9 GHz) in the far-IR to 50000 cm^{-1} (200 nm; 1.499 PHz) in the UV and

very high resolution down to 9×10^{-4} cm^{-1} (26.98 MHz) [16]. TDS can achieve 3 THz bandwidth and 1 GHz resolution via asynchronous optical sampling (ASOPS) [17,18].

Direct THz frequency-domain spectroscopy is comparatively less technologically mature, with few commercial systems produced [19]. Typically, these systems make use of free-running lasers, where the optically generated THz linewidth, and hence spectral resolution, is limited by the convolution of the two free-running laser spectral functions [20].

A spectroscopically measured absorbance curve depends on the convolution of the sample absorption and the spectrometer response. Deconvolution is possible, but in most cases, it is desirable to resolve the sample response without relying on noise-limited deconvolution processes [21]. Resolving a narrow spectral feature normally requires even sharper discrimination in the instrumentation illumination and detection. Analysis of the spectral line shape (SLS) provides information on the broadening mechanisms in both solid-state and gaseous samples. This is typically carried out through curve fitting of the measured spectrum using line shape models, which can introduce systematic errors particularly in the case of overlapping or closely spaced spectral lines [22,23].

Here we achieve four milestones. First, we demonstrate an ultra-high-resolution low-noise CW spectrometer. Second, we introduce a new platform for spectroscopy, where by software control of the illumination SLS, we can enhance the performance of a high-resolution CW spectrometer to reveal the details of closely spaced spectral peaks, with the potential to overcome the noise limits of conventional curve fitting. We achieve this enhancement by confirming the absorbance SLSs indirectly, not by their apparent shape but by analyzing the FWHM trend. Third, we demonstrate the technique by high-resolution spectroscopy on $LiYF_4:Ho^{3+}$, a material of interest for quantum science and technology, where we discriminate between inhomogeneous Gaussian and homogeneous Lorentzian contributions to absorption lines near 0.2 THz. And last, we generalize the concept to introduce the new idea of software-defined spectroscopy, enabled by the optical telecommunications toolbox [24], containing a large variety of readily available and low-cost photonic components.

The introduction of ultra-fast photodiodes such as the uni-traveling-carrier photodiodes (UTC-PDs) [25,26], initially for high-speed telecommunications, has allowed the generation of THz signals through photo-mixing. UTC-PDs mitigate the transit time response limited bandwidth of P-I-N photodiodes through blocking hole injection and facilitating the injection of hot electrons to the sweep-out layer. UTC-PD frequency response is limited only by the electron transit time and the time constant associated with the product of the load resistance and junction capacitance of the photodiode.

Early UTC-PD devices were vertically illuminated structures with a trade-off between optical responsivity and bandwidth [27]. In this geometry, the transit time response is improved by reduction of the absorber layer thickness. The reduction comes at the cost of reduced optical absorption in the photodiode absorption layer. There have been several structures that attempt to resolve this through the introduction of optical cavities [27] at the expense of more challenging fabrication.

Alternatively, the bandwidth/responsivity trade-off can be mitigated through the integration of the UTC-PD structure within an optical waveguide coupled photodiode [28]. In this case, the photodiode is evanescently coupled to a passive optical waveguide where the optical absorption and carrier transit direction are perpendicular to each other. This enables a thinner absorber layer to be used without a reduction in optical responsivity. Waveguide to chip coupling can be improved using optical mode converters to further enhance the optical responsivity of such edge coupled devices [29].

In this work, optical heterodyne generation of THz signals is achieved by the mixing of two optical tones f_1 and f_2 in a high-speed photodetector such as a UTC-PD. The resulting THz signal includes a strong component at the heterodyne frequency $|f_2 - f_1|$ with a SLS given by the convolution of the two free-running laser emission spectral functions. The THz signal can be tuned by varying f_1, f_2 or both. Typical semiconductor lasers have a significant linewidth due to fluctuations of the effective cavity length. Linewidths generally vary from 100 kHz for widely tunable external cavity diode lasers [30] to 2 MHz for distributed feedback (DFB) lasers [20].

To achieve the spectrally pure signals needed to resolve details such as SLS of electro-nuclear hyperfine absorption lines in solids and gases, we can exploit an optically phase correlated source for optical heterodyne generation of THz signals. This can be achieved through the use of an optical frequency comb (OFC), which generates a series of phase correlated lines with discrete frequency spacing.

Several methods have been proposed for the generation of OFCs, for example, Kerr combs using micro-resonators [31,32], mode-locked lasers [33], and fiber optic modulators. OFCs employing lithium niobate modulators [34–36] are attractive as comb sources due to the tunability of the center wavelength, and exact definition of the line spacing using a supplied microwave reference frequency. Use of such a modulator in a recirculating fiber loop with an erbium-doped fiber amplifier (EDFA) permits comb spans of over 2.7 THz [37]. Narrow-span combs with maximum flatness have also been achieved, initially through cascaded Mach–Zehnder and phase modulators [36,38].

Comb generation can be achieved in a more compact form by the use of a dual-drive Mach–Zehnder modulator, with comb spans up to 0.23 THz being demonstrated [39]. In this case, the construction of the comb is particularly compact and uses off-the-shelf telecommunications wavelength components while achieving a comb span suitable for accessing the region and resolution of interest for the lower-lying crystal field excitations (around 0.2 THz) in rare-earth salts such as $LiYF_4:Ho^{3+}$.

Demonstrations of CW spectroscopy based on OFC synthesis have been reported previously. In [40], a spectroscopic measurement is made of a gas sample using a super-continuum OFC. However, continuous constant power tuning was not achieved due to limitations of the fixed wavelength filtering used to select comb lines.

Other examples of THz synthesis for CW THz gas spectroscopy are reported in [41,42] and rely on the systems reported in [43,44]. In both of these reports, the system is based on phase locking of multiple external cavity lasers to multiple commercial reference OFCs based on mode-locked fiber lasers, making the system complex. Further, the linewidths of the synthesized THz signals are reported to be in the hundreds of kilohertz range, with frequency tuning steps of hundreds of kilohertz to megahertz, which limits the spectral resolution of the system. There are also many reports in the literature that demonstrate THz synthesis making use of

Table 1. Comparison of Continuous-Wave Frequency-Domain (CW FD) Spectrometer Performance with Literature and Commercial Systems

Reference	Type	Resolution	Continuously Tunable	Tuning Range
This work	CW FD	<100 Hz	Y	0.18 THz to 0.22 THz
Song *et al.* [40]	CW FD	<100 Hz	N	0.2 THz to 0.6 THz
Hindle *et al.* [43]	CW FD	520 kHz	Y	0.2 THz to 1.5 THz
A R Criado *et al.* [45]	CW FD	4 Hz	N	0.09 THz to 0.14 THz
Commercial photomixer -based spectrometer [19]	CW FD	<5 MHz	Y	0.1 THz to 2.5 THz
Commercial THz spectrometer extension system [46]	CW FD	20 MHz	Y	0.08 THz to 6 THz
Commercial VNA extenders [47]	CW FD	10 Hz	Y	Banded <1 octave

OFCs that make no demonstration of the application of the system for THz spectroscopy as in [45]. The system described in [45] is capable of semi-continuous tuning due only to the limitations in the bandwidth of the components used, and the stability of the optical injection locking.

The examples above have been summarized in Table 1 and help to illustrate the importance of both comb generation systems and comb line filtering in the realization of a fully tunable high-resolution spectroscopy system. We will show how off-the-shelf telecommunications components and programmable filters can be used to synthesize THz signals with software-defined line shapes, high spectral purity, and continuous tunability, limited only by the minimum tuning step size of the comb reference synthesizer, which can be $\ll$1 Hz.

There are many interesting solids, gases, and liquids with optical transitions in the THz region. There are also examples of engineered materials where a high spectral resolution is required to resolve high Q factor resonances. These include asymmetric split-ring resonances that support sharp Fano type resonances [48], and defect or guided modes in dielectric photonic crystal slabs [49,50]. Additionally, high Q factor resonances associated with bound states in the continuum observed in dielectric metamaterials as in [51–53] would also benefit from enhanced spectral resolution. Beyond direct measurement of high Q resonances, it is interesting to sense shifts in the frequency of the resonances from the introduction of either thin dielectric films [54] or bio-molecules [55]. To demonstrate the capabilities of our novel spectrometer, we have selected a material in the $LiYREF_4$ family, which has long fascinated the optics and quantum condensed matter communities in a variety of roles, from laser gain media [56] to platforms for fundamental research on Ising magnetism [57], coherent driven spin oscillations and many-body localization [58,59], entangled quantum states [60], and quantum phase transitions [61,62]. Rare-earth (RE)-doped materials have also been identified as candidates for quantum information applications [63–66]. There is particular interest in systems where electronuclear qubits can be read using optical transitions [67].

Single crystal yttrium lithium fluoride (YLF, $LiYF_4$) features a scheelite-structure, tetragonal space group C_{4h}^6. RE dopant substituting Y^{3+} at sites with S_4 symmetry causes insignificant crystalline structure perturbation [68]. The $4f^{10}$ electronic configuration of Ho^{3+}, a particularly popular dopant, is split into three by the Coulomb field and into five by spin–orbit coupling. We focus on the lower spin–orbit state $^5I_8$, which is further split by the crystal field. Karayianis identified this lowest level as a $\Gamma_{3,4}$ doublet and the two first excited states as Γ_2 singlets corresponding to absorption lines at 0.2 THz (7 cm^{-1}) and 0.7 THz (23 cm^{-1}) [69]. Electron-paramagnetic-resonance (EPR) experiments by Magariño determined the matrix elements coupling them [68,70]. We investigate the 0.2 THz transition from the $\Gamma_{3,4}$ doublet ground state to the first excited Γ_2 state. This work complements the study carried out by Matmon *et al.* [71], which was unable to measure the first excited state in the $^5I_8$ manifold due to limitations in the spectral range of the instrument used.

2. PROGRAMMABLE SPECTROSCOPY

We introduce the concept of *software-defined spectroscopy* as the exploitation of fast modulation of optical or RF signals to create illumination with bespoke spectral curves optimized to extract specific features of the sample optical response. Specific modulation patterns applied to simpler signals exploit common telecommunications technology to allow new and inexpensive approaches to access physical parameters that are difficult to determine with conventional spectroscopic techniques. Formally, as shown in Fig. 1, the mixing diode adds two optical communication inputs $\mathcal{A}_1(t)$, $\mathcal{A}_2(t)$, one modulated by the pattern generator $a_2(t)$, to produce THz radiation. Thus,

$$\mathcal{A}_1(t) = a_1 \exp(i(\omega_1 t)), \quad \mathcal{A}_2(t) = a_2(t) \exp(i(\omega_2 t + \phi)). \quad (1)$$

The photocurrent generated in the UTC-PD is proportional to the intensity $\mathcal{I}(t) \propto |\mathcal{A}(t)|^2$, implying an output spectrum for the UTC-PD:

$$\mathcal{I}(\omega) \propto |\mathcal{A}(\omega)|^2 \propto a_2(\omega) \otimes \delta(\omega - \Delta\omega), \quad (2)$$

where $\mathcal{A}(t) = \mathcal{A}_1(t) + \mathcal{A}_2(t)$, and δ is the Dirac delta function. The dominant current oscillation frequency is $\Delta\omega = \omega_1 - \omega_2$, as higher frequency components are filtered by the limited carrier speed. The spectrum measured at the detector $\mathcal{M}(\omega)$ is then simply the convolution of $\mathcal{I}(\omega)$ and the transmission spectrum $\mathcal{T}(\omega)$ of the sample and has the squared amplitude

$$|\mathcal{M}(\omega)|^2 \propto \left|a_2(\omega') \otimes \mathcal{T}(\omega' - \Delta\omega)\right|_\omega^2. \quad (3)$$

Equation (3) is the mathematical expression of the simplest type of software-defined spectroscopy that can be performed with our experimental arrangement.

The generation of the specific modulation patterns $a_2(t)$ was achieved through an inexpensive fiber optic intensity modulator (bandwidth <10 GHz) placed in one of the filtered comb

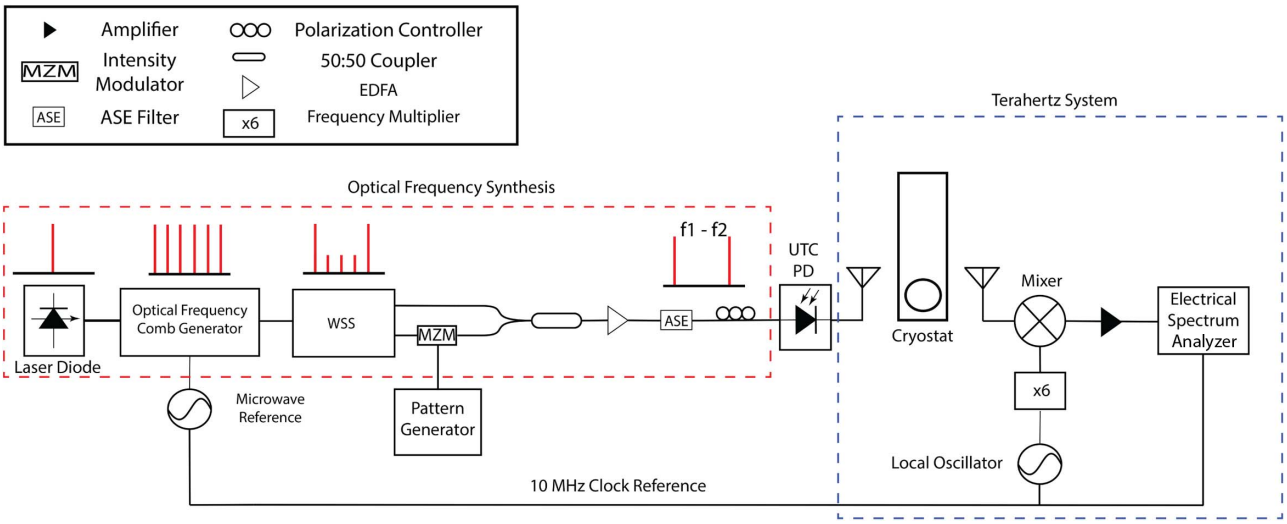

Fig. 1. Experiment schematic: a monochromatic telecommunications wavelength laser feeds an optical frequency comb generator (OFCG) with exact tunable spacing. A programmable wavelength selective switch (WSS) selects two bands 12 peaks apart, amplified and mixed in uni-traveling-carrier photodiode (UTC-PD). A 200 GHz beat frequency is transmitted through horn antennas and lenses through a continuous-flow liquid helium cryostat with thin polypropylene windows and $LiYF_4:Ho^{3+}$ sample. The received signal is down-converted using a sub-harmonic mixer and measured using a microwave spectrum analyzer.

line paths. There is very large flexibility in the choice of modulator. For example, replacing the intensity modulator with an in-phase quadrature-phase (IQ) modulator would allow a software-defined scan of transmission spectra using single-sideband suppressed-carrier modulation [72], without adjusting any other element (e.g., frequency comb) of the instrument. However, this would be limited by the maximum achievable modulator bandwidth. Another example is random on–off keying (OOK) modulation, which allows arbitrary broadening of the laser tone. The resulting spectrum can be approximated as a Gaussian broadening of the spectrum with a width defined by the time-base of the pulse pattern.

A more generalized broadening can be achieved when the OOK is defined as a two-state discrete Markov stochastic process defined by the transition matrix M and probability p:

$$M = \begin{pmatrix} p & 1-p \\ 1-p & p \end{pmatrix}. \tag{4}$$

We derive in Supplement 1 the exact analytical form of the spectra for a Markov OOK by calculating the correlation function and using the Wiener–Khintchin–Einstein theorem [73]. We recognize three cases that are of particular interest. Consider first $0 < p < 1/2$ with delaying correlation $\exp(\log(1-2p)t/\tau)$ and an exact Lorentzian power spectral density function (PSD); second, an unbiased pseudo-random bit sequence corresponding to a Markov process with $p = 1/2$ well approximated by a Gaussian PSD, with $\sigma = \sqrt{6}/\tau$; and finally, the case $1/2 < p < 1$ with oscillatory correlation $\exp(\log(1-2p)t/\tau)\cos(\pi t/\tau)$ featuring a side peak. By this technique, the modulated signal will be broadened and shifted by convolution with a spectrum that depends not only on the pattern time-base but also the digitally defined OOK defined by a state transition probability.

The digital OOK pattern is not limited to a Markovian process but could be any arbitrary bit sequence pattern. Here we focus only on exploiting the ability to generate both Gaussian and Lorentzian SLSs, achieved by tuning the value of p defining the Markovian OOK.

We are interested in obtaining the intrinsic SLS of the sample, distinguishing the Lorentzian homogeneous contribution from the Gaussian inhomogeneous contribution [74]. Consider the convolution of tuples of Gaussians $G_{\mu,\sigma}(f)$ and Lorentzians $L_{\mu,\gamma}(f)$:

$$G_{\mu_1,\sigma_1}(f) \otimes G_{\mu_2,\sigma_2}(f) = G_{\mu',\sigma'}(f), \tag{5a}$$

$$L_{\mu_1,\gamma_1}(f) \otimes L_{\mu_2,\gamma_2}(f) = L_{\mu',\gamma'}(f), \tag{5b}$$

$$L_{\mu_1,\gamma}(f) \otimes G_{\mu_2,\sigma}(f) = V_{\mu',\gamma,\sigma}(f), \tag{5c}$$

where $\mu' = \mu_1 + \mu_2$, $\gamma' = \gamma_1 + \gamma_2$, $\sigma' = \sqrt{\sigma_1^2 + \sigma_2^2}$, and $V_{\mu',\gamma,\sigma}(f)$ is the Voigt profile.

The corresponding FWHMs are

$$\Gamma_{G,G} = 2\sigma'\sqrt{2\ln 2}, \tag{6a}$$

$$\Gamma_{L,L} = 2\gamma', \tag{6b}$$

$$\Gamma_{L,G} \approx \sqrt{0.8664\gamma^2 + 8\sigma^2\log(2)} + 1.0692\gamma, \tag{6c}$$

where the last equation is the Olivero's Voigt width approximation [75]. Equations (6a)–(6c) and Fig. 2 reveal three distinguishable FWHM trends: a linear behavior for Lorentzian, root mean square (RMS) for Gaussian, and a more complex expression in between the former two for Voigt [76]. This observation opens possibilities of identifying a SLS that is not directly visible by examining the FWHM as a function of control parameters of the illumination SLS.

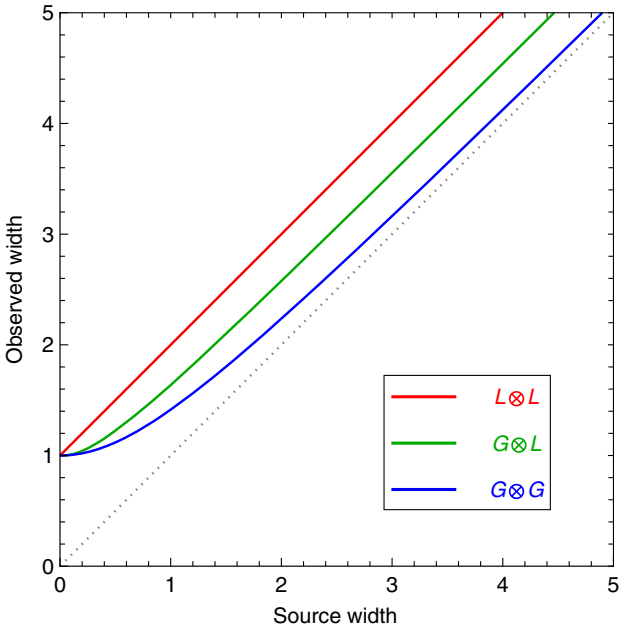

Fig. 2. Expected FWHM for three different convolution tuples. The convolution of two Lorentzians curves is also a Lorentzian with FWHM equal to the sum of its components and therefore appears as a linear curve (red). The convolution of two Gaussians is also a Gaussian curve with FWHM given by the RMS (blue). The convolution of Gaussian and Lorentzian curves gives a Voigt profile with FWHM in between (green).

3. METHODS

Figure 1 shows the experimental arrangement. Frequency synthesis was carried out using an OFC generator detailed by Shams *et al.* [77]. The comb is formed via modulation of a single 15 kHz linewidth laser signal at 1553.7 nm (RIO Orion Series). The modulator is a dual-drive Mach–Zehnder, driven by a microwave synthesizer, Rohde&Schwarz SMP04 40 GHz, which generates an optical comb spectrum with a flat response [39]. Comb line selection is achieved using a multi-port programmable optical filter (Finisar Waveshaper 4000S) with insertion loss 4.5 ± 0.1 dB, resulting in transmission of two coherent lines with 30 dB suppression of adjacent comb lines.

The two selected comb lines are amplified using an EDFA with a band-pass filter placed after the EDFA to reduce the noise contributions from amplified spontaneous emission (ASE). To achieve high-resolution tuning, the microwave synthesizer frequency is tuned across the frequency span between comb lines followed by sequentially shifting the programmable optical filtering band. A pause is introduced after changing filter settings, with a settling time of 500 ms. Figure 3(a) shows the synthesized OFC spectrum with a comb span of 0.27 THz, a comb line spacing of 17.25 GHz and two selected comb lines for a beat frequency of 207 GHz.

The UTC-PDs used in this study were grown by gas source molecular beam epitaxy by III-V laboratory; the epitaxial structure of the devices is detailed in [78]. The device geometry was a $3 \times 15\ \mu m^2$ with a 3 dB bandwidth of 90 GHz, and optical responsivity of 0.2 A/W. The UTC-PD was integrated with a co-planar waveguide, and the THz signal was extracted using a Cascade Microtech air co-planar (ACP) probe with a bandwidth of 140 GHz to 220 GHz. Flann 20 dB standard gain horn antennas (145 GHz to 220 GHz bandwidth) formed the free-space path within which the sample was placed.

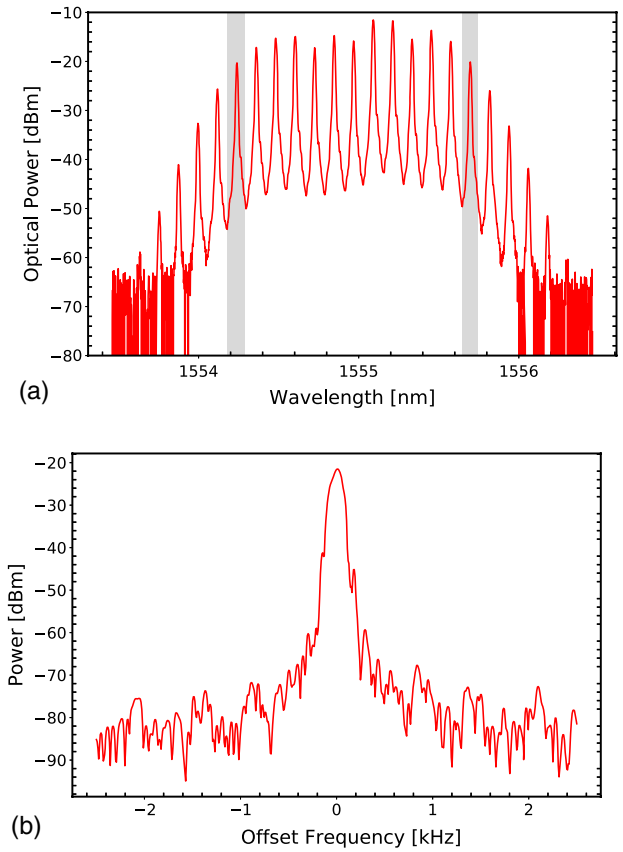

Fig. 3. Signal generation and detection. (a) Optical spectrum of the synthesized comb with tunable spacing (here 17.25 GHz); the highlighted peaks are selected with a waveshaper and then amplified, filtered, and mixed in a UTC-PD. (b) Down-converted IF signal from 207 GHz as measured by Agilent 8565E spectrum analyzer. The peak value is stored as the transmitted amplitude. Center frequency 15 GHz; resolution bandwidth 100 Hz.

The THz signal was down-converted using a sub-harmonic mixer (VDI WR5.1 SHM) with a bandwidth of 140 GHz to 220 GHz, driven by a ×6 frequency multiplier (OML S10MS-AG), supplying a LO signal between 70 GHz and 110 GHz. The LO frequency multiplier was driven by an Agilent E8257D 67 GHz signal generator. The THz signal was down-converted to a 15 GHz intermediate frequency (IF) and recorded on an Agilent 8565 E spectrum analyzer. A common 10 MHz reference clock is supplied to the LO signal generator and spectrum analyzer from the comb line reference synthesizer. Figure 2 shows the down-converted IF signal at a resolution bandwidth of 100 Hz. For resolution bandwidths <100 Hz, signal instabilities were noted. These can be attributed to frequency/phase-induced intensity noise arising from the unmatched optical path lengths traversed by the two optical tones before being heterodyned at the UTC-PD (Fig. 1). A significant improvement in signal stability can be achieved by active matching of the two optical path lengths, enabling signal stability at sub-hertz resolution bandwidths [37] to be maintained. Such resolution, however, was not required for the measurements reported here.

The sample of $LiYF_4$:Ho^{3+} was commercially provided by UAB ALTECHNA at 1% Ho^{3+} concentration, with custom dimensions of 10 mm × 10 mm × 2.18 mm. The crystals were cut and optically polished with the *c* axis parallel to one of the short

side lengths. The test sample was mounted on the cold finger of a continuous-flow liquid helium cryostat, and masks were inserted such that THz radiation could not be transmitted around the sample. The THz transmission through the sample was linearly polarized with the electrical field along the c crystalline axis. The cooled sample was illuminated through thin polypropylene windows, liquid helium was pulled by a diaphragm vacuum pump, and the sample temperature was maintained at 4 K or 200 K by an Oxford ITC4 controlling a resistive heater.

4. RESULTS

Figure 4(a) shows the composite raw spectral data acquired for the $LiYF_4$:Ho^{3+} at 4 K. This corresponds to the measured transmitted power normalized by the measured photocurrent. Each color indicates the range of data acquired for a single configuration of the waveshaper. The strong overall decaying trend is attributed to the UTC-PD frequency response and bandwidth limitations imposed by the ACP probe. The dips are due to the absorption lines of the sample. A similar curve was obtained for the same conditions with the $LiYF_4$:Ho^{3+} sample at 200 K and used as a reference for normalization and to estimate absorbance curves.

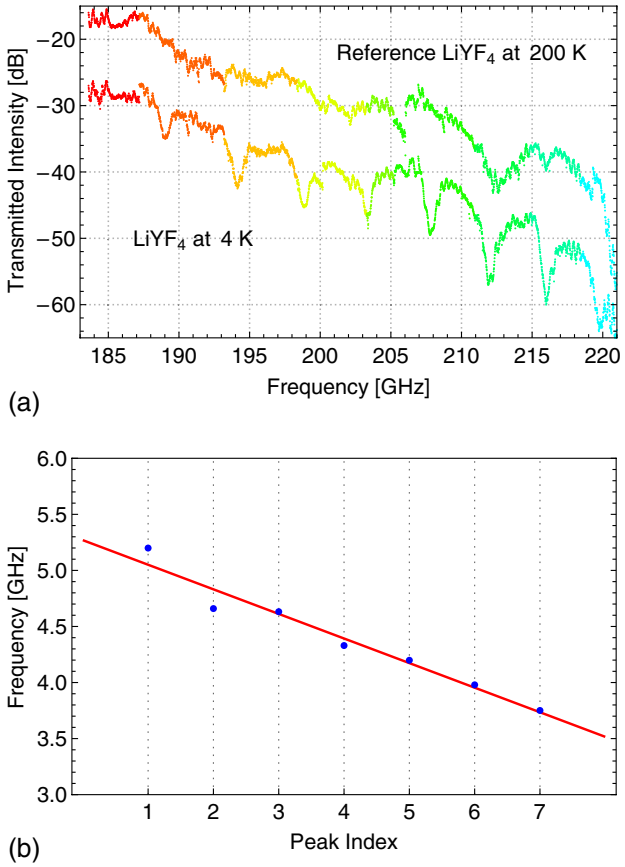

Fig. 4. $LiYF_4$:Ho^{3+} absorption data. (a) Raw data composite of measured transmitted intensity. Each color corresponds to the set of data points collected with the same waveshaper configuration. The downward trend corresponds to the emission and detection attenuation. The big dips on the bottom trace (4 K) correspond to the $LiYF_4$:Ho^{3+} sample absorptions not present in the top reference trace (shifted up 10 dB for convenience). The total time of acquisition was 20 min per scan. (b) Frequency difference between consecutive Hyperfine absorbance peaks is well described by a linear fit with slope -0.22 ± 0.02 GHz.

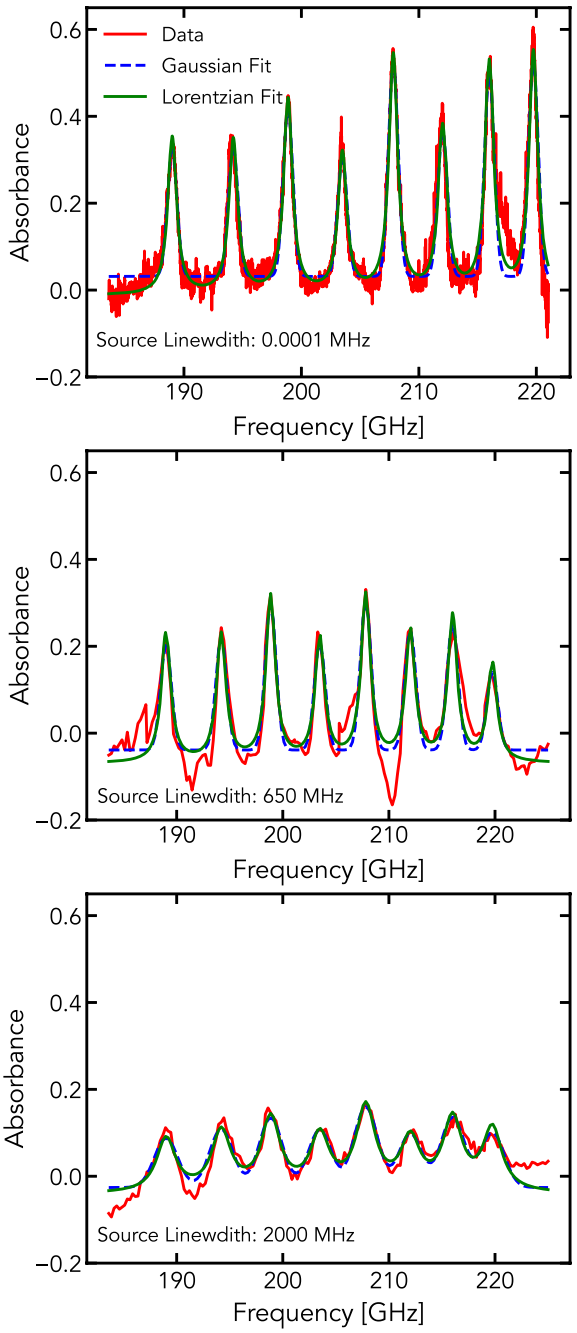

Fig. 5. Absorbance curves and respective fitting functions for a selection of illuminations with different spectral linewidths. The top plot is for the narrowest (100 Hz) instrumental linewidth. As the illumination spectra broaden, so do the absorption spectra. The blue and green lines are the convolutions of Gaussians and Lorentzians, respectively, of width as defined in the limit where source FWHM$- > 0$ (see Figs. 2 and 6) with the illumination spectra.

At 200 K, absorption peaks are no longer measurable as higher states are thermally populated, and the weak absorption peaks have been flattened by Doppler broadening. We observe eight absorption lines in the range between 189 GHz and 220 GHz with linearly decreasing spacing ranging from 5.2 GHz to 3.75 GHz, with slope -219 ± 20 MHz [Fig. 4(b)]. We attribute the spacing variation to the second-order hyperfine shift {Eq. (10) in [71]}.

The absorption line appears broader than the experimental resolution, an effect that we next examine quantitatively.

We use Gaussian broadening applied to the THz signal by the optical modulator and measure the FWHM of the estimated absorbance curves as a function of the illumination linewidth. Figure 5 shows three representative cases for source linewidths of 100 Hz, 650 MHz, and 2000 MHz and the respective Gaussian fits; the artificial broadening of the illumination SLS allows us to observe a nonlinear FWHM trend featuring a narrow 99% confidence band for the RMS fit. The FWHM increases with the illumination broadening, revealing an RMS trend as expected for convolutions of two Gaussian SLSs [Eq. (5a)]. The trend shows an excellent RMS fit ($w_m = \sqrt{w_i^2 + w_s^2}$) of the absorbance FWHM as a function of illumination FWHM (w_i), yielding a sample linewidth $w_s = 0.907 \pm 0.017$ GHz. The trend in Fig. 6 is characteristic of the convolution of two Gaussian SLSs. This implies an intrinsically Gaussian line shape caused by inhomogeneous broadening, ruling out state lifetime as a significant contributor to the absorption linewidth. Consistent with this result, an attempt to fit the data in Fig. 6 with the Voigt result Eq. (6c) reveals a negligible Lorentzian contribution (FWHM $= 2\gamma' = 0.0004 \pm 10.3$ MHz), corresponding to an excited state lifetime bounded from below by 30 ns. Furthermore, if the observed 0.907 GHz FWHM were to be attributed to a purely Lorentzian hypothesis, the expected FWHM curve would show a considerable departure from the identity asymptote and the observed linewidth, as shown in Fig. 6 (black line). The curve instead follows the Gaussian form indicated by the blue line in Fig. 2, or equivalently, a Voigt trend but with a negligible offset (and therefore Lorentzian contribution) from the blue line. For comparison of our novel modulator-based spectroscopy to traditional methodology, we have performed numerically intensive fitting to a Voigt line shape of the simple unmodulated absorption measured with our ultra-high-resolution spectrometer. The "best" fits using conventional analysis are obtained for the Lorentzian ($\chi^2 = 1.1$) rather than Gaussian limit ($\chi^2 = 1.5$), a finding influenced by the selection of the weighting factors for the multi-peak spectrum and the details of the data between peaks and therefore not a robust estimation of the underlying physics. Concomitantly, visual inspection reveals a negligible difference between Gaussian and Lorentzian descriptions and the data, while the dependence of the unbiased (by choices of weighting) FWHM on the modulator-introduced Gaussian broadening incontrovertibly shows that the correct Voigt description is dominated by the Gaussian term.

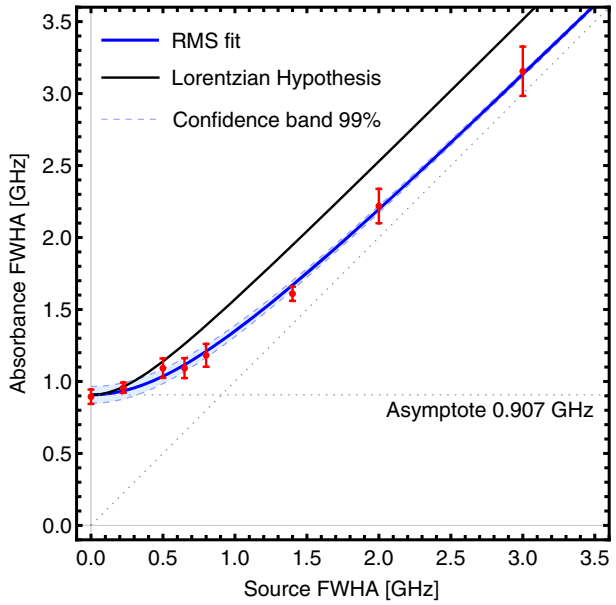

Fig. 6. Measured absorbance FWHM (w_m) illumination FWHM (w_i) is well fitted by an RMS model $\sqrt{w_i^2 + w_s^2}$, with a sample FWHM $w_s = 0.907 \pm 0.017$ GHz. The markers correspond to FWHM estimations for the whole trace (eight peaks) with error bars showing the standard error. The thin lines around the fit confine the 99% confidence band. Two dotted gray lines represent the two asymptotes of the fitting function, a constant of 0.907 GHz, and the identity function of slope 1. The black curve is expected if the 0.907 GHz sample broadening were to be attributed to a Lorentzian. The information in this figure clearly indicates that both source and sample intrinsic SLSs are Gaussian. See Supplement 1.

5. PERFORMANCE COMPARISON

A key benefit of coherent THz generation demonstrated here is an improvement in the spectral purity of the incoming THz signal. In this experiment, low-phase-noise synthesizers have been used to drive the OFC generator, and to provide the LO for down-conversion. As discussed in the Methods section, the measured IF FWHM linewidth was <100 Hz, implying a quality factor Q of $>2 \times 10^9$. The linewidth measurement was limited by low-frequency noise observed at resolution bandwidths <100 Hz.

The measured noise of each of the synthesizers and the down-converted IF signal were −104 dBc and −78 dBc at 10 kHz offset, respectively (Fig. 7). The measured noise of the down-converted signal represents the overall system noise as described in [37], which includes the scaled phase noise of the comb reference synthesizer $[S1 + 20\log_{10}(N1)]$ (dBc/Hz) and the LO $[S2 + 20\log_{10}(N2)]$ (dBc/Hz) contribution from the comb/heterodyne system and the spectrum analyzer. S1 and S2 are the phase noise of the reference synthesizer and LO, respectively, at the fundamental frequencies of −104 dBc and −105.75 dBc for S1 and S2, and N1 and N2 are the frequency multiplication factors.

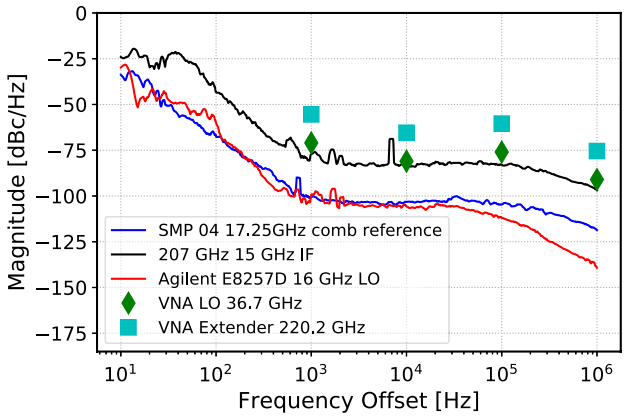

Fig. 7. Measured phase noise. Black: 207 GHz after down-conversion to IF Comb, IF synthesizers, and down-converted IF signal. Red: Agilent E8257D at 16 GHz. Blue: Rohd&Schwarz SMP04 at 17.25 GHz. Rhomboid green markers: high-performance commercial VNA 36.7 GHz, Cyan square markers: high-performance commercial VNA with frequency extender 220.2 GHz.

The spacing between the optical lines used to generate the heterodyne frequency of 207 GHz is equal to 12 comb line spacings ($N1 = 12$). Further, a second-harmonic mixer with a $\times 6$ frequency multiplier (Virginia Diodes WR5.1 SHM) was used to down-convert the signal, $N2 = 12$. Hence, the increase in the composite noise of $\sim$26 dB in the down-converted signal is due predominantly to the frequency multiplication factor $20\log_{10}(12)$, and the composite noise contribution from the comb/heterodyne system is estimated to be -89.5 dBc at 10 kHz offset. High-performance vector network analyzers (VNAs) are sometimes used for high-resolution spectroscopy in the sub-THz regime [79,80] and for verification of TDS data [81].

The phase noise level achieved through optical synthesis at 207 GHz is better than high-performance commercial network analyser systems with frequency extenders for the equivalent frequency band, as shown in Fig. 7. The comparison points (green and cyan markers) are derived from the specified phase noise of the network analyzer and the multiplication factor of the extender only, without allowance for excess noise from system integration and are therefore best-case estimates. It should, however, be noted that frequency extenders can deliver milliwatt-level output powers compared to microwatt-level output powers from the UTC-PD used in this work, so they are better suited to spectroscopy of samples at high temperatures (i.e., where beam heating is not a problem). Frequency extender sources also do not offer the software-defined line shape capabilities of the photonically generated THz sources such as UTC-PDs, and have limited tuning ranges less than one octave when compared to antenna integrated UTC-PDs with substrate integrated lenses, which can be multi-octave [82]. We observe a signal-to-noise ratio (SNR) of 50 dB for the 207 GHz signal down-converted to an IF of 15 GHz.

Besides the frequency precision, our system is capable of high-frequency accuracy, by referencing the microwave synthesizer to primary frequency standards via global positioning system (GPS) disciplined sources. Low-power monochromatic illumination also allows minimum perturbation of the state of the sample, with negligible heating and perturbation of the population of the states.

Some of the existing experimental limitations derive from compromises for flexibility at the research stage, and no attempts to improve acquisition rates were performed. At the same time, they set a well-defined agenda for future development. The unpackaged UTC-PD required a fiber launcher to couple the focused laser beams into the device, making it susceptible to drift. Continuous monitoring of the photocurrent allowed continuous optimization of the alignment and normalization of the observed curve for the small fluctuations observed. The output power available from UTC-PDs is limited primarily by thermal effects, while the bandwidth is limited by electron transit time and RC constraints. In addition to these bandwidth constraints, additional limitations are imposed on the device by the electronic circuitry connected to the device. For this experiment, we utilized a UTC-PD integrated with a co-planar waveguide. To extract the THz signals from the device, we used an ACP probe with a WR-5 waveguide, along with a standard gain horn antenna. Such probes and antennas have a discrete bandwidth limitation imposed by the cut-off frequencies of the waveguide geometry. These limitations can be better managed through the use of devices integrated with planar broadband antennas, which remove the need for external probes to extract the THz signals [83,84]. In this experiment, only the amplitude of the power transmitted was recorded. The system could be extended by exploiting a photonically generated LO. Utilizing a self-heterodyne configuration such as that of Hisatake *et al.* [85] where one of the coherent lines is shifted in frequency and then used to down-convert to a low-frequency IF would enable the recovery of both amplitude and phase information from the spectrometer. Also, it would eliminate additional linewidth broadening introduced by the LO frequency multiplication step. The reference signal for spectrum normalization neglects small changes in the sample reflections as a consequence of temperature variations of the sample refraction index.

6. CONCLUSION

We have demonstrated a novel software-defined, photonic CW THz spectrometer that offers continuous tuning and sub-100 Hz linewidth. The system has the potential to reach sub-hertz resolution with an electronic feedback loop to actively match the heterodyne optical path lengths. The capabilities of the new approach are illustrated by high-resolution spectroscopy of $LiYF_4$:Ho^{3+} at 4 K, which complements measurements by Matmon *et al.* [71] for a band unreachable by FTIR with conventional sources. The spectral features of the transitions in the $^5I_8$ spin–orbit state have been resolved to reveal the magnitude of the second-order hyperfine splitting (-0.22 ± 0.02 GHz) by direct optical observation. The spacing between adjacent hyperfine lines is shown to vary linearly through the octet, revealing the magnitude of the second-order hyperfine shift [Eq. (10) in [71]}. Furthermore and more importantly, we demonstrate the use of the software-defined spectroscopy technique to determine that the absorbance SLS is predominantly Gaussian and as such, likely due to inhomogeneous broadening; therefore, the intrinsic state lifetimes are much longer than the inverse linewidth. We estimate a lower bound on the excited state lifetime of $\tau > 30$ ns from the Lorentzian contribution of the Voigt fitting (FWHM $= 2\gamma' = 0.0004 \pm 10.3$ MHz). We conclude that the deliberate control of the instrument line shape via a key component of the optical communications toolbox—the modulator—enables reliable determination of spectral shapes. The technique depends on the underlying physics rather than on the fitting of model parameters, and can be applied much more generally to identifying specific spectral features because it allows the construction of sequences of essentially arbitrary illumination spectra (i.e., basis functions) for their optimal isolation. For example, illumination spectra with multiple peaks at variable positions could be used as "rulers" to measure sideband positions in absorption spectra.

Funding. Schweizerischer Nationalfonds zur Förderung der Wissenschaftlichen Forschung; European Research Council (Project HERO, 810451); Engineering and Physical Sciences Research Council (EP/J017671/1, EP/P021859/1).

Acknowledgment. RIH and HS thank Guy Matmon and Joshua Freeman for valuable discussion.

Disclosures. RIH, HS, AJS, and GA declare financial interest relating to a patent application for the concept of software-defined spectroscopy.

See Supplement 1 for supporting content.

REFERENCES

1. S. S. Dhillon, M. S. Vitiello, E. H. Linfield, A. G. Davies, M. C. Hoffmann, J. Booske, C. Paoloni, M. Gensch, P. Weightman, G. P. Williams, E. Castro-Camus, D. R. S. Cumming, F. Simoens, I. Escorcia-Carranza, J. Grant, S. Lucyszyn, M. Kuwata-Gonokami, K. Konishi, M. Koch, C. A. Schmuttenmaer, T. L. Cocker, R. Huber, A. G. Markelz, Z. D. Taylor, V. P. Wallace, J. A. Zeitler, J. Sibik, T. M. Korter, B. Ellison, S. Rea, P. Goldsmith, K. B. Cooper, R. Appleby, D. Pardo, P. G. Huggard, V. Krozer, H. Shams, M. Fice, C. Renaud, A. Seeds, A. Stöhr, M. Naftaly, N. Ridler, R. Clarke, J. E. Cunningham, and M. B. Johnston, "The 2017 terahertz science and technology roadmap," J. Phys. D **50**, 43001 (2017).
2. A. J. Seeds, M. J. Fice, K. Balakier, M. Natrella, O. Mitrofanov, M. Lamponi, M. Chtioui, F. van Dijk, M. Pepper, G. Aeppli, A. G. Davies, P. Dean, E. Linfield, and C. C. Renaud, "Coherent terahertz photonics," Opt. Express **21**, 22988–23000 (2013).
3. H. Hintzsche and H. Stopper, "Effects of terahertz radiation on biological systems," Crit. Rev. Environ. Sci. Technol. **42**, 2408–2434 (2012).
4. U. U. Graf, C. E. Honingh, K. Jacobs, and J. Stutzki, "Terahertz heterodyne array receivers for astronomy," J. Infrared Millim. Terahertz Waves **36**, 896–921 (2015).
5. A. J. Seeds, H. Shams, M. J. Fice, and C. C. Renaud, "Terahertz photonics for wireless communications," J. Lightwave Technol. **33**, 579–587 (2015).
6. P. T. Greenland, S. A. Lynch, A. F. G. van der Meer, B. N. Murdin, C. R. Pidgeon, B. Redlich, N. Q. Vinh, and G. Aeppli, "Coherent control of Rydberg states in silicon," Nature **465**, 1057–1061 (2010).
7. J. R. Hoh, C. E. Groppi, and J. V. Siles, "New developments for integrated Schottky receivers in the terahertz regime," Proc. SPIE **10708**, 170–177 (2018).
8. Th. de Graauw, F. P. Helmich, T. G. Phillips, J. Stutzki, E. Caux, N. Whyborn, P. Dieleman, P. R. Roelfsema, H. Aarts, R. Assendorp, R. Bachiller, W. Baechtold, A. Barcia, D. A. Beintema, V. Belitsky, A. O. Benz, R. Bieber, A. Boogert, C. Borys, B. Bumble, P. Cas, M. Caris, P. Cerulli-Irelli, G. Chattopadhyay, S. Cherednichenko, M. Ciechanowicz, O. Coeur-Joly, C. Comito, A. Cros, A. de Jonge, G. de Lange, B. Delforges, Y. Delorme, T. den Boggende, J.-M. Desbat, C. Diez-González, A. M. Di Giorgio, L. Dubbeldam, K. Edwards, M. Eggens, N. Erickson, J. Evers, M. Fich, T. Finn, B. Franke, T. Gaier, C. Gal, J. R. Gao, J.-D. Gallego, S. Gauffre, J. J. Gill, S. Glenz, H. Golstein, H. Goulooze, T. Gunsing, R. Güsten, P. Hartogh, W. A. Hatch, R. Higgins, E. C. Honingh, R. Huisman, B. D. Jackson, H. Jacobs, K. Jacobs, C. Jarchow, H. Javadi, W. Jellema, M. Justen, A. Karpov, C. Kasemann, J. Kawamura, G. Keizer, D. Kester, T. M. Klapwijk, Th. Klein, E. Kollberg, J. Kooi, P.-P. Kooiman, B. Kopf, M. Krause, J.-M. Krieg, C. Kramer, B. Kruizenga, T. Kuhn, W. Laauwen, R. Lai, B. Larsson, H. G. Leduc, C. Leinz, R. H. Lin, R. Liseau, G. S. Liu, A. Loose, I. López-Fernandez, S. Lord, W. Luinge, A. Marston, and J. Martn-Pintado, et al., "The Herschel-heterodyne instrument for the far-infrared (HIFI)," Astron. Astrophys. **518**, L6 (2010).
9. A. Wootten and A. R. Thompson, "The Atacama large millimeter/submillimeter array," Proc. IEEE **97**, 1463–1471 (2009).
10. C. Risacher, V. Vassilev, R. Monje, I. Lapkin, V. Belitsky, A. Pavolotsky, M. Pantaleev, P. Bergman, S.-E. Ferm, E. Sundin, M. Svensson, M. Fredrixon, D. Meledin, L.-G. Gunnarsson, M. Hagström, L.-Å. Johansson, M. Olberg, R. Booth, H. Olofsson, and L.-Å. Nyman, "A 0.8 mm heterodyne facility receiver for the apex telescope," Astron. Astrophys. **454**, L17–L20 (2006).
11. M. C. Wiedner, G. Wieching, F. Bielau, K. Rettenbacher, N. H. Volgenau, M. Emprechtinger, U. U. Graf, C. E. Honingh, K. Jacobs, B. Vowinkel, K. M. Menten, L.-Å. Nyman, R. Güsten, S. Philipp, D. Rabanus, J. Stutzki, and F. Wyrowski, "First observations with condor, a 1.5 THz heterodyne receiver," Astron. Astrophys. **454**, L33–L36 (2006).
12. P. Pütz, C. E. Honingh, K. Jacobs, M. Justen, M. Schultz, and J. Stutzki, "Terahertz hot electron bolometer waveguide mixers for great," Astron. Astrophys. **542**, L2 (2012).
13. L. Jiang, S. Shiba, T. Shiino, K. Shimbo, N. Sakai, T. Yamakura, Y. Irimajiri, P. G. Ananthasubramanian, H. Maezawa, and S. Yamamoto, "Development of 1.5 THz waveguide NbTiN superconducting hot electron bolometer mixers," Supercond. Sci. Technol. **23**, 045025 (2010).
14. S. Schiller, B. Roth, F. Lewen, O. Ricken, and M. Wiedner, "Ultra-narrow-linewidth continuous-wave THz sources based on multiplier chains," Appl. Phys. B **95**, 55–61 (2009).
15. B. Stuart, *Infrared Spectroscopy* (American Cancer Society, 2015), pp. 1–18.
16. Bruker, *The IFS 125HR FTIR Spectrometer* (2018).
17. P. A. Elzinga, R. J. Kneisler, F. E. Lytle, Y. Jiang, G. B. King, and N. M. Laurendeau, "Pump/probe method for fast analysis of visible spectral signatures utilizing asynchronous optical sampling," Appl. Opt. **26**, 4303–4309 (1987).
18. A. Bartels, R. Cerna, C. Kistner, A. Thoma, F. Hudert, C. Janke, and T. Dekorsy, "Ultrafast time-domain spectroscopy based on high-speed asynchronous optical sampling," Rev. Sci. Instrum. **78**, 035107 (2007).
19. D. Stanze, A. Deninger, A. Roggenbuck, S. Schindler, M. Schlak, and B. Sartorius, "Compact CW terahertz spectrometer pumped at 1.5 μm wavelength," J. Infrared Millim. Terahertz Waves **32**, 225–232 (2011).
20. K. Balakier, H. Shams, M. J. Fice, L. Ponnampalam, C. S. Graham, C. C. Renaud, and A. J. Seeds, "Optical phase lock loop as high-quality tuneable filter for optical frequency comb line selection," J. Lightwave Technol. **36**, 4646–4654 (2018).
21. J. K. Kauppinen, D. J. Moffatt, H. H. Mantsch, and D. G. Cameron, "Fourier self-deconvolution: a method for resolving intrinsically overlapped bands," Appl. Spectrosc. **35**, 271–276 (1981).
22. V. Kochanov, "On systematic errors in spectral line parameters retrieved with the Voigt line profile," J. Quant. Spectrosc. Radiat. Transf. **113**, 1635–1641 (2012).
23. V. Kochanov and I. Morino, "Methane line shapes and spectral line parameters in the 5647-6164 cm^{-1} region," J. Quant. Spectros. Radiat. Transf. **206**, 313–322 (2018).
24. T. Nagatsuma, G. Ducournau, and C. C. Renaud, "Advances in terahertz communications accelerated by photonics," Nat. Photonics **10**, 371–379 (2016).
25. T. Ishibashi, N. Shimizu, S. Kodama, H. Ito, T. Nagatsuma, and T. Furuta, "Uni-traveling-carrier photodiodes," in *Ultrafast Electronics and Optoelectronics 1997 Topical Meeting Technical Digest*, Vol. **13** (Optical Society of America, 1997), pp. 83–87.
26. E. Rouvalis, M. J. Fice, C. C. Renaud, and A. J. Seeds, "Optoelectronic detection of millimetre-wave signals with travelling-wave uni-travelling carrier photodiodes," Opt. Express **19**, 2079–2084 (2011).
27. P. Latzel, F. Pavanello, M. Billet, S. Bretin, A. Beck, M. Vanwolleghem, C. Coinon, X. Wallart, E. Peytavit, G. Ducournau, M. Zaknoune, and J. Lampin, "Generation of MW level in the 300-GHz band using resonant-cavity-enhanced unitraveling carrier photodiodes," IEEE Trans. Terahertz Sci. Technol. **7**, 800–807 (2017).
28. C. C. Renaud, M. Robertson, D. Rogers, R. Firth, P. J. Cannard, R. Moore, and A. J. Seeds, "A high responsivity, broadband waveguide uni-travelling carrier photodiode," Proc. SPIE **6194**, 61940C (2006).
29. E. Rouvalis, C. C. Renaud, D. G. Moodie, M. J. Robertson, and A. J. Seeds, "Traveling-wave uni-traveling carrier photodiodes for continuous wave THz generation," Opt. Express **18**, 11105–11110 (2010).
30. M. Alalusi, P. Brasil, S. Lee, P. Mols, L. Stolpner, A. Mehnert, and S. Li, "Low noise planar external cavity laser for interferometric fiber optic sensors," Proc. SPIE **7316**, 235–247 (2009).
31. P. Del'Haye, A. Schliesser, O. Arcizet, T. Wilken, R. Holzwarth, and T. J. Kippenberg, "Optical frequency comb generation from a monolithic microresonator," Nature **450**, 1214–1217 (2007).
32. M. Kues, C. Reimer, J. M. Lukens, W. J. Munro, A. M. Weiner, D. J. Moss, and R. Morandotti, "Quantum optical microcombs," Nat. Photonics **13**, 170–179 (2019).
33. H. Sanjoh, H. Yasaka, Y. Sakai, K. Sato, H. Ishii, and Y. Yoshikuni, "Multiwavelength light source with precise frequency spacing using a mode-locked semiconductor laser and an arrayed waveguide grating filter," IEEE Photon. Technol. Lett. **9**, 818–820 (1997).
34. K. Ho and J. M. Kahn, "Optical frequency comb generator using phase modulation in amplified circulating loop," IEEE Photon. Technol. Lett. **5**, 721–725 (1993).
35. S. Bennett, B. Cai, E. Burr, O. Gough, and A. J. Seeds, "1.8-THz bandwidth, zero-frequency error, tunable optical comb generator for DWDM applications," IEEE Photon. Technol. Lett. **11**, 551–553 (1999).
36. M. Kourogi, T. Enami, and M. Ohtsu, "A monolithic optical frequency comb generator," IEEE Photon. Technol. Lett. **6**, 214–217 (1994).
37. L. Ponnampalam, M. Fice, H. Shams, C. Renaud, and A. Seeds, "Optical comb for generation of a continuously tunable coherent THz signal from 122.5 GHz to 2.7 THz," Opt. Lett. **43**, 2507–2510 (2018).
38. Y. Takita, F. Futami, M. Doi, and S. Watanabe, "Highly stable ultra-short pulse generation by filtering out flat optical frequency components," in *Conference on Lasers and Electro-Optics/International*

Quantum Electronics Conference and Photonic Applications Systems Technologies (Optical Society of America, 2004), paper CTuN1.
39. T. Sakamoto, T. Kawanishi, and M. Izutsu, "Widely wavelength-tunable ultra-flat frequency comb generation using conventional dual-drive Mach-Zehnder modulator," Electron. Lett. **43**, 1039–1040 (2007).
40. H.-J. Song, N. Shimizu, T. Furuta, K. Suizu, H. Ito, and T. Nagatsuma, "Broadband-frequency-tunable sub-terahertz wave generation using an optical comb, AWGS, optical switches, and a uni-traveling carrier photodiode for spectroscopic applications," J. Lightwave Technol. **26**, 2521–2530 (2008).
41. C. Bray, A. Cuisset, F. Hindle, G. Mouret, R. Bocquet, and V. Boudon, "Spectral lines of methane measured up to 2.6 THz at sub-MHz accuracy with a CW-THz photomixing spectrometer: line positions of rotational transitions induced by centrifugal distortion," J. Quant. Spectrosc. Radiat. Transf. **203**, 349–354 (2017).
42. Y.-D. Hsieh, H. Kimura, K. Hayashi, T. Minamikawa, Y. Mizutani, H. Yamamoto, T. Iwata, H. Inaba, K. Minoshima, F. Hindle, and T. Yasui, "Terahertz frequency-domain spectroscopy of low-pressure acetonitrile gas by a photomixing terahertz synthesizer referenced to dual optical frequency combs," J. Infrared Millim. Terahertz Waves **37**, 903–915 (2016).
43. F. Hindle, G. Mouret, S. Eliet, M. Guinet, A. Cuisset, R. Bocquet, T. Yasui, and D. Rovera, "Widely tunable THz synthesizer," Appl. Phys. B **104**, 763 (2011).
44. T. Yasui, H. Takahashi, Y. Iwamoto, H. Inaba, and K. Minoshima, "Continuously tunable, phase-locked, continuous-wave terahertz generator based on photomixing of two continuous-wave lasers locked to two independent optical combs," J. Appl. Phys. **107**, 033111 (2010).
45. A. R. Criado, C. de Dios, E. Prior, G. H. Döhler, S. Preu, S. Malzer, H. Lu, A. C. Gossard, and P. Acedo, "Continuous-wave sub-THz photonic generation with ultra-narrow linewidth, ultra-high resolution, full frequency range coverage and high long-term frequency stability," IEEE Trans. Terahertz Sci. Technol. **3**, 461–471 (2013).
46. Bruker, "Vertera THz extension," 2017, https://www.bruker.com/products/infrared-near-infrared-and-raman-spectroscopy/terahertz/vertera.html.
47. T. Crowe, B. Foley, S. Durant, D. Koller, K. Hui, J. Hesler, S. Singh, and K. Anderson, "Instrumentation for metrology from MMW to THz," in *Proc. 4th UK/EU-China Workshop Millim. Wave Terahertz Technol.* (University of Virginia, 2011), pp. 1–37.
48. C. Jansen, I. A. I. Al-Naib, N. Born, and M. Koch, "Terahertz metasurfaces with high Q-factors," Appl. Phys. Lett. **98**, 051109 (2011).
49. Z. Jian, J. Pearce, and D. M. Mittleman, "Defect modes in photonic crystal slabs studied using terahertz time-domain spectroscopy," Opt. Lett. **29**, 2067–2069 (2004).
50. C. Kyaw, R. Yahiaoui, Z. A. Chase, V. Tran, A. Baydin, F. Tay, J. Kono, M. Manjappa, R. Singh, D. C. Abeysinghe, A. M. Urbas, and T. A. Searles, "Guided-mode resonances in flexible 2D terahertz photonic crystals," Optica **7**, 537–541 (2020).
51. S. Han, L. Cong, Y. K. Srivastava, B. Qiang, M. V. Rybin, A. Kumar, R. Jain, W. X. Lim, V. G. Achanta, S. S. Prabhu, Q. J. Wang, Y. S. Kivshar, and R. Singh, "All-dielectric active terahertz photonics driven by bound states in the continuum," Adv. Mater. **31**, 1901921 (2019).
52. D. R. Abujetas, N. van Hoof, S. ter Huurne, J. G. Rivas, and J. A. Sánchez-Gil, "Spectral and temporal evidence of robust photonic bound states in the continuum on terahertz metasurfaces," Optica **6**, 996–1001 (2019).
53. W. Zhang, A. Charous, M. Nagai, D. M. Mittleman, and R. Mendis, "Characterizing optical resonances using spatial mode reshaping," Optica **5**, 1414–1417 (2018).
54. Y. K. Srivastava, R. T. Ako, M. Gupta, M. Bhaskaran, S. Sriram, and R. Singh, "Terahertz sensing of 7 nm dielectric film with bound states in the continuum metasurfaces," Appl. Phys. Lett. **115**, 151105 (2019).
55. C. Weisenstein, D. Schaar, A. K. Wigger, H. Schäfer-Eberwein, A. K. Bosserhoff, and P. H. Bolívar, "Ultrasensitive THz biosensor for PCR-free CDNA detection based on frequency selective surfaces," Biomed. Opt. Express **11**, 448–460 (2020).
56. A. Santo, A. Librantz, L. Gomes, P. Pizani, I. Ranieri, N. Vieira, and S. Baldochi, "Growth and characterization of $LiYF_4$:Nd single crystal fibres for optical applications," J. Cryst. Growth **292**, 149–154 (2006).
57. D. H. Reich, B. Ellman, J. Yang, T. F. Rosenbaum, G. Aeppli, and D. P. Belanger, "Dipolar magnets and glasses: neutron-scattering, dynamical, and calorimetric studies of randomly distributed Ising spins," Phys. Rev. B **42**, 4631–4644 (1990).
58. S. Ghosh, R. Parthasarathy, T. F. Rosenbaum, and G. Aeppli, "Coherent spin oscillations in a disordered magnet," Science **296**, 2195–2198 (2002).
59. D. M. Silevitch, C. Tang, G. Aeppli, and T. F. Rosenbaum, "Tuning high-Q nonlinear dynamics in a disordered quantum magnet," Nat. Commun. **10**, 4001 (2019).
60. S. Ghosh, T. F. Rosenbaum, G. Aeppli, and S. N. Coppersmith, "Entangled quantum state of magnetic dipoles," Nature **425**, 48–51 (2003).
61. D. Bitko, T. F. Rosenbaum, and G. Aeppli, "Quantum critical behavior for a model magnet," Phys. Rev. Lett. **77**, 940–943 (1996).
62. H. M. Rønnow, R. Parthasarathy, J. Jensen, G. Aeppli, T. F. Rosenbaum, and D. F. McMorrow, "Quantum phase transition of a magnet in a spin bath," Science **308**, 389–392 (2005).
63. J. Brooke, "Quantum annealing of a disordered magnet," Science **284**, 779–781 (1999).
64. J. Brooke, T. F. Rosenbaum, and G. Aeppli, "Tunable quantum tunnelling of magnetic domain walls," Nature **413**, 610–613 (2001).
65. S. Bertaina, S. Gambarelli, A. Tkachuk, I. N. Kurkin, B. Malkin, A. Stepanov, and B. Barbara, "Rare-earth solid-state qubits," Nat. Nanotechnol. **2**, 39 (2007).
66. F. Bussières, C. Clausen, A. Tiranov, B. Korzh, V. B. Verma, S. W. Nam, F. Marsili, A. Ferrier, P. Goldner, H. Herrmann, C. Silberhorn, W. Sohler, M. Afzelius, and N. Gisin, "Quantum teleportation from a telecom-wavelength photon to a solid-state quantum memory," Nat. Photonics **8**, 775 (2014).
67. M. Rančić, M. P. Hedges, R. L. Ahlefeldt, and M. J. Sellars, "Coherence time of over a second in a telecom-compatible quantum memory storage material," Nat. Phys. **14**, 50 (2017).
68. J. Magariño, J. Tuchendler, J. P. D'Haenens, and A. Linz, "Submillimeter resonance spectroscopy of Ho3+ in lithium yttrium fluoride," Phys. Rev. B **13**, 2805–2808 (1976).
69. N. Karayianis, D. E. Wortman, and H. P. Jenssen, "Analysis of the optical spectrum of Ho^{3+} in $LiYF_4$," J. Phys. Chem. Solids **37**, 675–682 (1976).
70. T. Magariño, J. Tuchendler, P. Beauvillain, and I. Laursen, "EPR experiments in $LiTbF_4$, $LiHoF_4$, and $LiErF_4$ at submillimeter frequencies," Phys. Rev. B **21**, 18–28 (1980).
71. G. Matmon, S. A. Lynch, T. F. Rosenbaum, A. J. Fisher, and G. Aeppli, "Optical response from terahertz to visible light of electronuclear transitions in $LiYF_4$:Ho^{3+}," Phys. Rev. B **94**, 205132 (2016).
72. H. Shams, K. Balakier, L. Gonzalez-Guerrero, M. J. Fice, L. Ponnampalam, C. S. Graham, C. C. Renaud, and A. J. Seeds, "Optical frequency tuning for coherent THz wireless signals," J. Lightwave Technol. **36**, 4664–4670 (2018).
73. A. Khintchine, "Korrelationstheorie der stationären stochastischen prozesse," Math. Annalen **109**, 604–615 (1934).
74. W. Koechner, *Solid-State Laser Engineering*, Springer series in optical sciences (Springer Berlin Heidelberg, 2013).
75. J. J. Olivero and R. L. Longbothum, "Empirical fits to the Voigt line width: a brief review," J. Quant. Spectrosc. Radiat. Transf. **17**, 233–236 (1977).
76. J. He and Q. Zhang, "Discussion on the full width at half maximum (FWHM) of the Voigt spectral line," Optik **124**, 5245–5247 (2013).
77. H. Shams, M. J. Fice, L. Gonzalez-Guerrero, C. C. Renaud, F. van Dijk, and A. J. Seeds, "Sub-THz wireless over fiber for frequency band 220–280 GHz," J. Lightwave Technol. **34**, 4786–4793 (2016).
78. E. Rouvalis, M. Chtioui, M. Tran, F. Lelarge, F. van Dijk, M. J. Fice, C. C. Renaud, G. Carpintero, and A. J. Seeds, "High-speed photodiodes for InP-based photonic integrated circuits," Opt. Express **20**, 9172–9177 (2012).
79. C. Caspers, V. P. Gandhi, A. Magrez, E. de Rijk, and J.-P. Ansermet, "Sub-terahertz spectroscopy of magnetic resonance in $BiFeO_3$ using a vector network analyzer," Appl. Phys. Lett. **108**, 241109 (2016).
80. E. Dadrasnia, S. Puthukodan, V. V. K. Thalakkatukalathil, H. Lamela, G. Ducournau, J.-F. Lampin, F. Garet, and J.-L. Coutaz, "Sub-THz characterisation of monolayer graphene," J. Spectrosc. **2014**, 601059 (2014).
81. M. Naftaly, N. Ridler, J. Molloy, N. Shoaib, and D. Stokes, "A comparison method for THz measurements using VNA and TDS," in *40th International Conference on Infrared, Millimeter, and Terahertz waves (IRMMW-THz)* (2015), pp. 1–2.
82. C. C. Renaud, M. Natrella, C. Graham, J. Seddon, F. Van Dijk, and A. J. Seeds, "Antenna integrated THz uni-traveling carrier photodiodes," IEEE J. Sel. Top. Quantum Electron. **24**, 8500111 (2018).

83. H. Ito, F. Nakajima, T. Furuta, and T. Ishibashi, "Continuous {THz}-wave generation using antenna-integrated uni-travelling-carrier photodiodes," Semicond. Sci. Technol. **20**, S191–S198 (2005).
84. E. Rouvalis, C. C. Renaud, D. G. Moodie, M. J. Robertson, and A. J. Seeds, "Continuous wave terahertz generation from ultra-fast InP-based photodiodes," IEEE Trans. Microw. Theory Tech. **60**, 509–517 (2012).
85. S. Hisatake, J. Kim, K. Ajito, and T. Nagatsuma, "Self-heterodyne spectrometer using uni-traveling-carrier photodiodes for terahertz-wave generators and optoelectronic mixers," J. Lightwave Technol. **32**, 3683–3689 (2014).